

# Correlational Effects of the Molecular-Tilt Configuration and the Intermolecular van der Waals Interaction on the Charge Transport in the Molecular Junction

Jaeho Shin,<sup>†</sup> Kyungyeol Gu,<sup>‡</sup> Seunghoon Yang,<sup>†</sup> Chul-Ho Lee,<sup>†</sup> Takhee Lee,<sup>§</sup> Yun Hee Jang,<sup>\*,†,§</sup> and Gunuk Wang<sup>\*,†,§</sup>

<sup>†</sup>KU-KIST Graduate School of Converging Science and Technology, Korea University, 145 Anam-ro, Seongbuk-gu, Seoul 02841, Republic of Korea

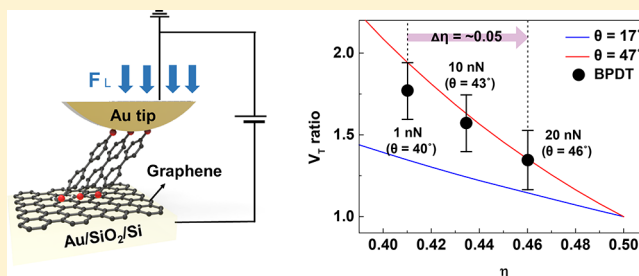
<sup>‡</sup>Department of Energy Science and Engineering, DGIST, Daegu 42988, Republic of Korea

<sup>§</sup>Department of Physics and Astronomy, and Institute of Applied Physics, Seoul National University, Seoul 08826, Republic of Korea

## Supporting Information

**ABSTRACT:** Molecular conformation, intermolecular interaction, and electrode–molecule contacts greatly affect charge transport in molecular junctions and interfacial properties of organic devices by controlling the molecular orbital alignment. Here, we statistically investigated the charge transport in molecular junctions containing self-assembled oligophenylene molecules sandwiched between an Au probe tip and graphene according to various tip-loading forces ( $F_L$ ) that can control the molecular-tilt configuration and the van der Waals (vdW) interactions. In particular, the molecular junctions exhibited two distinct transport regimes according to the  $F_L$  dependence (i.e.,  $F_L$ -dependent and  $F_L$ -independent tunneling regimes). In addition, the charge-injection tunneling barriers at the junction interfaces are differently changed when the  $F_L \leq 20$  nN. These features are associated to the correlation effects between the asymmetry-coupling factor ( $\eta$ ), the molecular-tilt angle ( $\theta$ ), and the repulsive intermolecular vdW force ( $F_{vdW}$ ) on the molecular-tunneling barriers. A more-comprehensive understanding of these charge transport properties was thoroughly developed based on the density functional theory calculations in consideration of the molecular-tilt configuration and the repulsive vdW force between molecules.

**KEYWORDS:** Molecular junction, graphene, molecular-tilt configuration, intermolecular van der Waals interaction, transition voltage



The energy-level alignment of the molecular frontier orbitals, the highest-occupied molecular orbital (HOMO) and the lowest-occupied molecular orbital (LUMO), with the Fermi level of electrodes ( $E_F$ ) is essential for understanding the charge transport in molecular-scale junctions as well as the development of organic electronic devices.<sup>1–9</sup> These molecular frontier-orbital levels that are between both of the electrodes form the charge-injection barriers that represent the transmission channels, which can play a key role in the determining of the electrical characteristic of the molecular junction.<sup>3–7,10</sup> Diverse factors such as molecular-backbone structures,<sup>11</sup> molecular-anchoring groups,<sup>6</sup> the  $E_F$  of electrodes,<sup>6,8</sup> and the coordination geometries and coupling strengths at the electrode–molecule contacts<sup>12</sup> could all impact the interfacial transmission barrier, and the corresponding engineering is crucial for the attainment of desirable molecular and organic-device performances.<sup>9</sup>

Furthermore, a change of the molecular conformation can also significantly affect the transport channel, leading to a large variability of the electrical properties of the molecular junction in which even identical junctional constituents such as molecules and electrodes are formed.<sup>13–17</sup> Diverse stimuli

such as light,<sup>18</sup> electric fields,<sup>19</sup> heat,<sup>20</sup> and mechanical stress<sup>21–23</sup> have been utilized to change the static structure of the molecular conformation. In particular, the mechanical stress-driven conformational control using a scanning probe microscopy (SPM) technique can lead to a direct dynamic variation of the molecular structure itself.<sup>14,15,17,21,23</sup> This technique is very useful in an investigation of the effect of the molecular-tilt configuration on the electrical properties of a single or bundle molecular junction. This is because the metal-probe tip can be directly applied to the molecules to change the molecular-tilt angle ( $\theta$ ) using a tip-loading force ( $F_L$ ) or an adjustment of the junction displacement with respect to the surface normal.<sup>14,15,17</sup> Recently, Kim et al. found that, by using the scanning tunneling microscope-based breaking junction technique (STM-BJ), the HOMO resonance-transmission curve in a single benzenediamine molecular junction can be shifted close to the  $E_F$  when the  $\theta$  is increased by pulling the

Received: March 30, 2018

Revised: June 15, 2018

Published: June 15, 2018

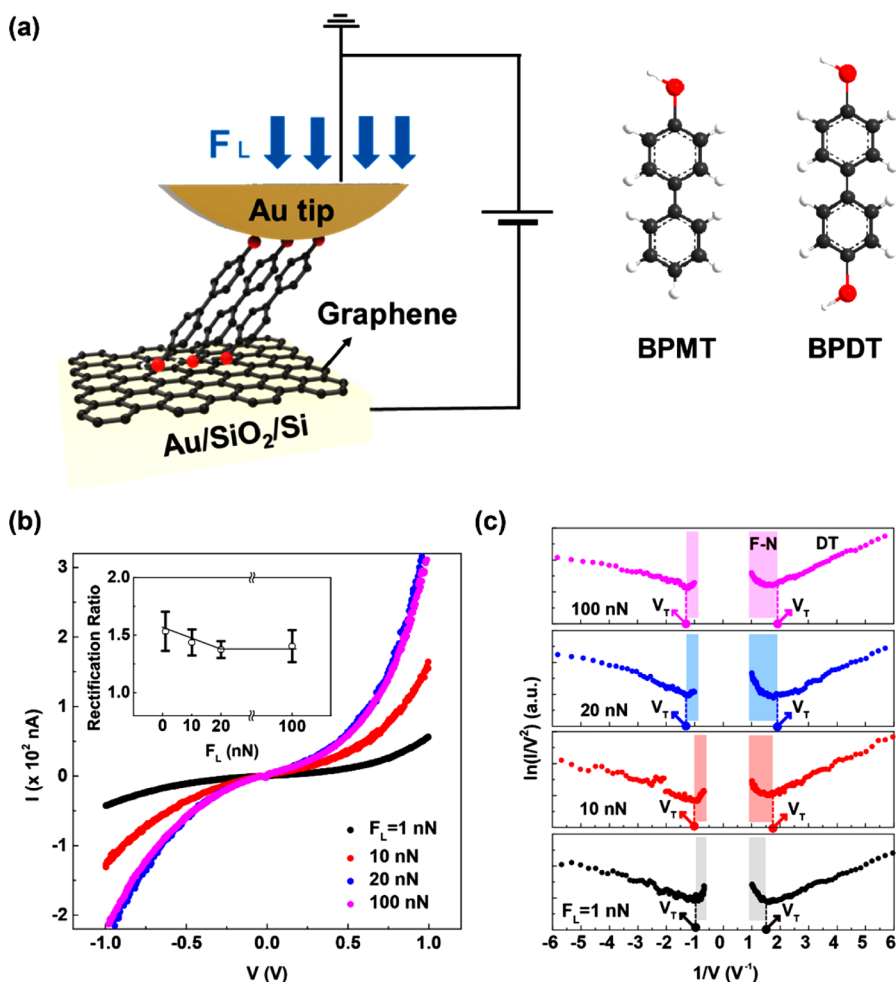


**Figure 1.** (a) (left) Schematic of a molecular junction composed of a Au/OPT SAMs/graphene film stacked on an Au/SiO<sub>2</sub>/Si substrate under an  $F_L$  of the Au tip using the CAFM technique. (Right) The molecular structures for (i) BPMT and (ii) BPDT are shown. (b) Representative  $I$ – $V$  plots of BPDT junction at  $F_L = 1, 10, 20,$  and  $100$  nN, respectively. Inset shows the plot of the rectification ratio, which was obtained using  $|I(V = 1 \text{ V})/I(V = -1 \text{ V})|$  as a function of  $F_L$ . (c) Representative F–N plots of BPDT junction at  $F_L = 1, 10, 20,$  and  $100$  nN, respectively. Arrows indicate  $V_T$  values corresponding to the transition from DT to F–N tunneling at different  $F_L$  values.

junction.<sup>17</sup> As a result, the electrode–molecule coupling was increased with the increased  $\theta$ . The HOMO energy level ( $E_{\text{HOMO}}$ ) that is shifted by the molecular-tilt configuration can lead to an enhancement of the charge transport and the smaller junction asymmetry.<sup>17</sup> The increased coupling and the shifted HOMO level had been explained based on density functional theory (DFT) calculation considering the different tilt angles.<sup>17</sup> In the case of the bundle molecular junction that is based on self-assembled monolayers (SAMs) of molecules, however, the numerous van der Waals (vdW) interactions that inevitably exist between the molecules might cause a distinctive electrical behavior that would not be observed in a single molecular circuit.<sup>24</sup> For example, Nerngchamnonng et al. demonstrated that the vdW interaction between the ferrocene-alkanethiolate molecules in the EGaIn-based junction is majorly responsible for the variability of the transport conduction depending on the  $n_{\text{even}}$  and the  $n_{\text{odd}}$  in the alkyl-backbone structure ( $-\text{[CH}_2\text{]}_n-$ ), namely, the odd–even effect.<sup>24</sup> Generally, the magnitude of the vdW interactions depends on the chain-to-chain intermolecular distance ( $d_{\text{cc}}$ ), so it is expected to be strongly correlated to the molecular-tilt configuration of the SAMs.<sup>14,15,25</sup> Although a number of experiments have separately verified the effects of the asymmetric coupling, the

molecular-tilt configuration, or the vdW interaction on the charge transfer through a molecular layer, a comprehensive understanding of the way that the electrical characteristic varies with the correlation between among these effects is not yet established. In addition, the measurements and theoretical predictions regarding the way that the molecular orbital alignment is changed by these correlations have rarely been investigated.

Here, we report the influences of the contact coupling, molecular-tilt configuration, and intermolecular vdW interaction on the charge transports through oligophenylene-based monothiol and dithiol (denoted as OPT) molecular junctions that are sandwiched between Au probe tip and graphene using a conductive atomic force microscopy (CAFM) technique. We found that the change in the charge-injection tunneling barriers that are formed at the junction interfaces and the asymmetric ratio of the barriers are strongly associated with the correlational effects between the asymmetry-coupling factor ( $\eta$ ), the molecular-tilt angle ( $\theta$ ), and the repulsive intermolecular vdW force ( $F_{\text{vdW}}$ ). Also, a comparison of the tunneling-barrier experiment results and those of a theoretical estimation that is based on the DFT calculation depending on

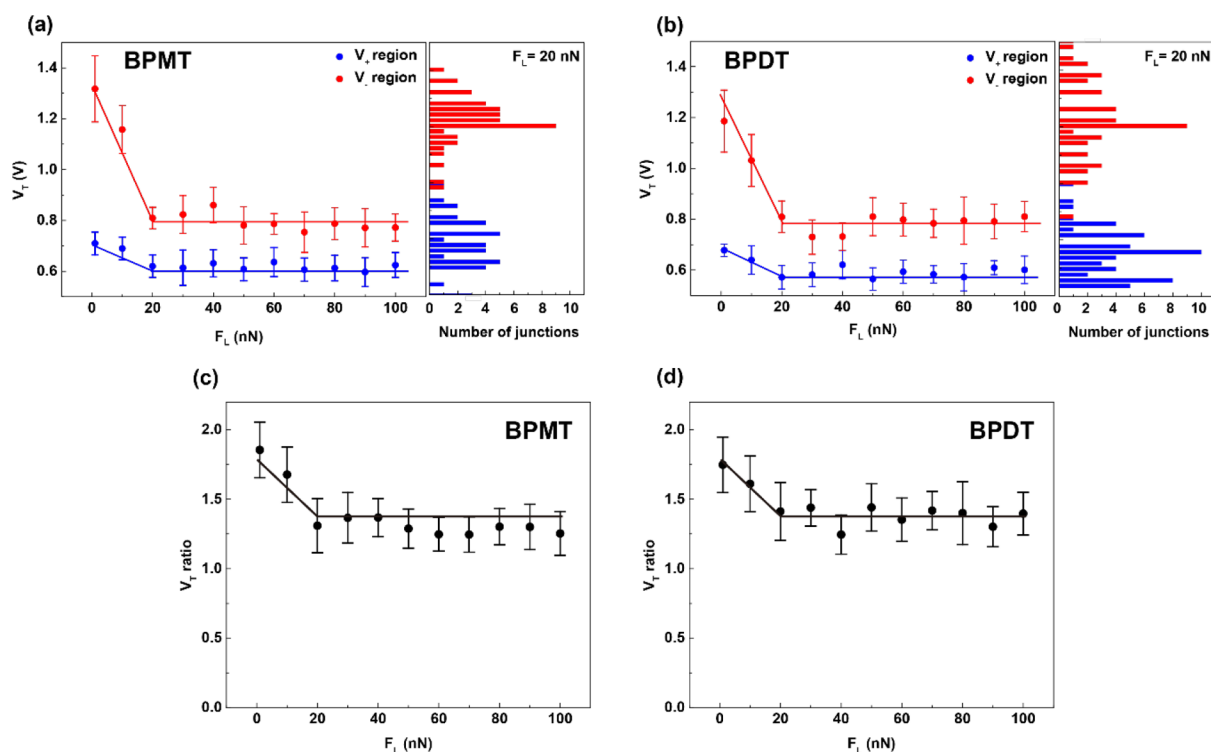


**Figure 2.** (a, b) Experimentally obtained  $V_T$  plotted as functions of the  $F_L$  and the voltage polarities ( $V_+$  and  $V_-$ ) for BPMT and BPDT molecular junctions, respectively. The error bars indicate the standard deviations of each  $V_T$  ( $\sim 500$  measurements in total). The right side of panels a and b show examples of  $V_T$  histograms at  $F_L = 20$  nN for BPMT and BPDT molecular junctions, respectively. Each histogram plot was obtained from 35–50 individual  $I$ – $V$  measurements. (c, d) Experimentally obtained  $V_T$  ratios, defined as  $|V_T(V_-)|/|V_T(V_+)|$ , plotted as a function of  $F_L$  for BPMT and BPDT molecular junctions, respectively.

the  $\theta$  was made, and it is confirmed that both are in sound agreement.

**Results and Discussion.** Figure 1a shows a schematic diagram of the completed molecular junction employing an Au probe tip/OPT SAMs/graphene stack on an Au/SiO<sub>2</sub>/Si substrate, where the  $F_L$  was controlled using the CAFM technique. Self-assembled OPT molecular layers with different numbers of the thiol groups (i) biphenyl-4-monothiol (BPMT) and (ii) biphenyl-4,4'-dithiol (BPDT) were used as the transport channels. The details of the experimental method, the optimal packing structure of the OPT SAMs, and the estimation of the contacted molecular numbers are described in the Methods section. Figure 1b shows the representative current–voltage ( $I$ – $V$ ) characteristics for the BPDT molecular junction according to different  $F_L$  values. They all show the typical tunneling behavior, which mainly originates from the energy-level offset between the  $E_F$  of the electrodes and the nearest molecular orbital levels (HOMO and LUMO levels).<sup>4–8,26</sup> In the junction fabricated without OPT SAMs, direct Au–graphene contact was consistently made regardless of  $F_L$ , thereby leading to the identical electrical short due to metallic contacts (Figure S1). In contrast, the junction fabricated with OPT SAMs did not show any electrical shorts, not even when the  $I$ – $V$  characteristics were measured under  $F_L = 100$  nN, thereby excluding the possibility of direct Au–graphene contact in our molecular junctions. Generally, the main charge-transport mechanism in the junction containing the OPT molecules is known for HOMO-mediated nonresonant tunneling that means the hole is the major carrier.<sup>6,26</sup> Interestingly, the average tunneling-current level of the BPDT junction under the same

$F_L$  is approximately 1 order of magnitude lower than that of the BPMT (Figure S2). This current difference can be explained by the following two factors: (i) the BPMT length (10.5 Å) is slightly smaller than that of the BPDT (11.9 Å), thereby resulting in a shorter tunneling length; and (ii) the graphene does not form a chemisorbed contact with a thiol group (–SH).<sup>27,28</sup> As shown in Figure 1b, the  $I$ – $V$  characteristics show clearly asymmetric tunneling behaviors and their rectification ratio that is defined as  $|I(+1\text{ V})/I(-1\text{ V})|$  was decreased from  $1.53 \pm 0.17$  to  $1.38 \pm 0.07$  when  $F_L$  was increased from 1 to 20 nN. When  $F_L \geq 20$  nN, however, the rectification ratio is barely changed regardless of  $F_L$ . Similarly, this asymmetry had been also observed in the molecular junction consisting of symmetric amine-terminated oligophenyl molecules that were sandwiched between graphite and an Au electrode.<sup>17</sup> In the case of the Au/BPDT/Au structure, however, the  $I$ – $V$  characteristic exhibits a symmetric behavior (Figure S3); considering this, the asymmetric phenomenon might be mainly associated with the asymmetric coupling between graphene and the Au electrode and not with the molecular structure itself. Another noticeable feature is the presence of two distinct transport regimes according to the  $F_L$  dependence. For example, the tunneling currents show that the  $F_L$ -dependent characteristic when the  $F_L$  is in the range of 1–20 nN, whereas they show the  $F_L$ -independent characteristic when  $F_L \geq 20$  nN, as shown in Figure 1b.

To analyze the charge-injection tunneling barriers in the molecular junction, the transition voltage spectroscopy (TVS) profile that exploits the plot of the  $\ln(I/V^2)$  versus the  $1/V$ , named the Fowler–Nordheim (F–N) plot, was investigated regarding both voltage polarities.<sup>3,5,15,29,30</sup> The local minimum

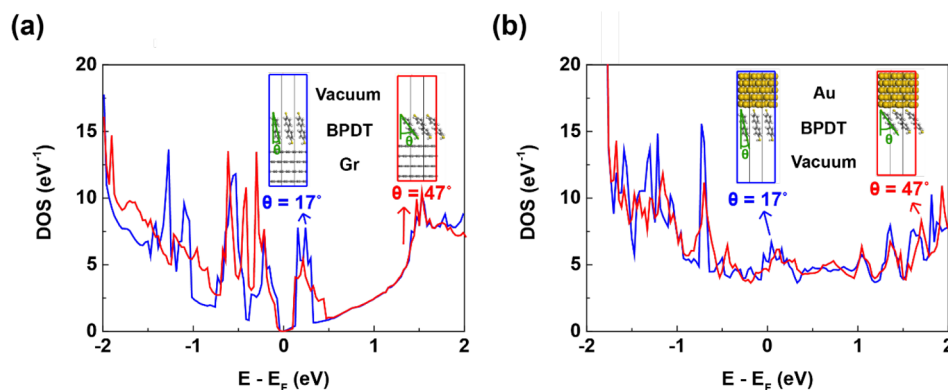


**Figure 3.** DOS curves for (a) graphene (Gr) and BPDT near the Fermi level  $E_F$  ( $-3.9$  eV) and for (b) Au and BPDT near the Fermi level  $E_F$  ( $-4.9$  eV) at  $\theta = 17$  (blue) and  $47^\circ$  (red).

in the F–N plot represents the transition voltage ( $V_T$ ) from direct tunneling (DT) to F–N tunneling transport, which provides intuitive information regarding the tunneling barrier height, as shown in Figure 1c.<sup>3,5,15</sup> Similar to the tunneling currents, the two  $V_T$  regimes are also distinguished according to the  $F_L$  dependence. Under  $F_L \leq 20$  nN, the F–N tunneling regime that is selectively marked in the colored background gradually widened regardless of the voltage polarities, thereby lowering the  $V_T$ , as the  $F_L$  was increased from 1 to 20 nN; however, this regime remained unaffected at the  $F_L \geq 20$  nN, resulting in a constant  $V_T$ , as shown in Figure 1c. Furthermore, over the entire range of  $F_L$ , it was observed that  $V_T$  in the negative-voltage region (denoted as the  $V_-$  region) is higher in the positive-voltage region (denoted as the  $V_+$  region), implying the asymmetric transport barriers at the junction interfaces. Because the asymmetric coupling between graphene/SH and Au–S is inherently established in that junction, the different hole-injection barrier heights ( $\Phi_h$ ) that were formed at those contacts could be responsible for the asymmetric  $V_T$  behavior, as discussed later. These phenomena were commonly observed in the BPMT molecular junctions as well (Figure S4). Merging the graphs in Figure 1c clarifies the shifts in the  $V_T$  (Figure S5).

To statistically analyze those electrical properties, a characterization of a significantly large number of the  $I$ – $V$  data ( $\sim 500$  measurements in total) according to the  $F_L$  was performed. Figure 2a,b shows the statistical  $V_T$  plots for the BPMT and BPDT molecular junctions as functions of  $F_L$  and the voltage polarities ( $V_+$  and  $V_-$ ), respectively. The values for the mean and the standard deviation of the  $V_T$  corresponding to each  $F_L$  were obtained from the individual  $I$ – $V$  measurements on at least 35–50 junction positions. As an example of the  $V_T$  values at  $F_L = 20$  nN, the  $V_T$  statistical histograms are shown in the right sides of panels a and b of Figures 2. The deviation in  $V_T$  might be due to different contact geometries, electrical stress-induced deformation, or different Au-tip curvature radii.<sup>28</sup> As shown in panels a and b of Figure 2, the experimental  $V_T$  values in the  $V_-$  (or  $V_+$ ) regions for the BPMT and BPDT junctions were decreased from  $1.32 \pm 0.13$  V (or  $0.71 \pm 0.04$  V) to  $0.80 \pm 0.06$  V (or  $0.62 \pm 0.04$  V) and from  $1.19 \pm 0.12$  V (or  $0.67 \pm 0.03$  V) to  $0.81 \pm 0.06$  V (or  $0.56 \pm 0.05$  V) when the  $F_L$  was increased from 1 to 20 nN, respectively. Notably, the slope of the  $V_T$  line in the  $V_-$  region was slightly steeper than that of the  $V_T$  line in the  $V_+$  region, implying less-asymmetric coupling as the  $F_L$  was increased from 1 to 20 nN. In the case of  $20 \text{ nN} \leq F_L \leq 100 \text{ nN}$ ;

however, the  $V_T$  values for both junctions are nearly unchanged regardless of the voltage-sweep polarities ( $V_+$  and  $V_-$ ). Panels c and d of Figure 2 show the  $V_T$  ratios that are defined as  $|V_T(V_-)|/|V_T(V_+)|$  for both the BPMT and BPDT molecular junctions as a function of  $F_L$ , respectively. As mentioned previously, the asymmetric  $V_T$  behavior arises from a difference of the asymmetric coupling between both interfaces of the molecular junction.<sup>3,30</sup> Generally, the influence of the voltage polarities on the  $V_T$  is strongly related to the degree of the asymmetry in a molecular junction,<sup>3</sup> so the  $V_T$  ratio can be used to quantify them. As shown in panels c and d of Figure 2, the experimental  $V_T$  ratio for BPMT and BPDT molecular junctions decreased from  $1.85 \pm 0.20$  to  $1.31 \pm 0.19$  and from  $1.71 \pm 0.20$  to  $1.40 \pm 0.21$ , respectively, when the  $F_L$  was increased from 1 to 20 nN. At  $F_L \geq 20$  nN, however,  $V_T$  ratios for BPMT and BPDT molecular junctions were almost independent of the  $F_L$  magnitude and found to be  $1.30 \pm 0.05$  and  $1.38 \pm 0.07$ , respectively. This result can support the following two claims: (i) because the  $V_T$  ratio reflects the degree of asymmetry between two electrodes at molecular junctions, a decreased  $V_T$  ratio indicates less asymmetry in the range of  $F_L \leq 20$  nN, while it is barely changed in the range of  $F_L \geq 20$  nN; and (ii) the strengths of the physisorbed contact couplings (graphene/CH versus graphene/SH) in the BPMT and BPDT molecular junctions are similar. We also investigated the electrical characteristics of the lower-packing-density OPT molecular junction sandwiched between the Au tip and graphene for various  $F_L$  (Figure S6). Although the lower-packing-density and densely packed OPT molecular junctions (Figure 2) showed similar  $V_T$  ratio behaviors, those of the lower-packing-density OPT molecular junction were lower than those of the densely packed one, and the onset of the  $V_T$  plateau of the lower-packing-density OPT molecular junction occurred at lower  $F_L < 20$  nN, as suggested by the difference in the molecular-tilt configuration and the magnitude of the molecular-packing-density-dependent mechanical stress measured under the same  $F_L$  (Figure S6).

To elucidate the origins of the asymmetric  $V_T$  behavior and the change in the  $V_T$  ratio, the density of states (DOS) and DFT-based  $T(E)$  were calculated for bundled OPT molecular junctions for  $\theta = 17$  and  $47^\circ$  and for various  $\eta$ . The details of theoretical DFT calculations are described in the Methods section and Figures S7 and S8. Note that  $\theta = 17^\circ$  corresponds to the initial state without an applied  $F_L$ , and  $\theta = 47^\circ$  corresponds to  $F_L = 27$  nN based on the Hertzian elastic contact model (see Table S1). The DOS of graphene and

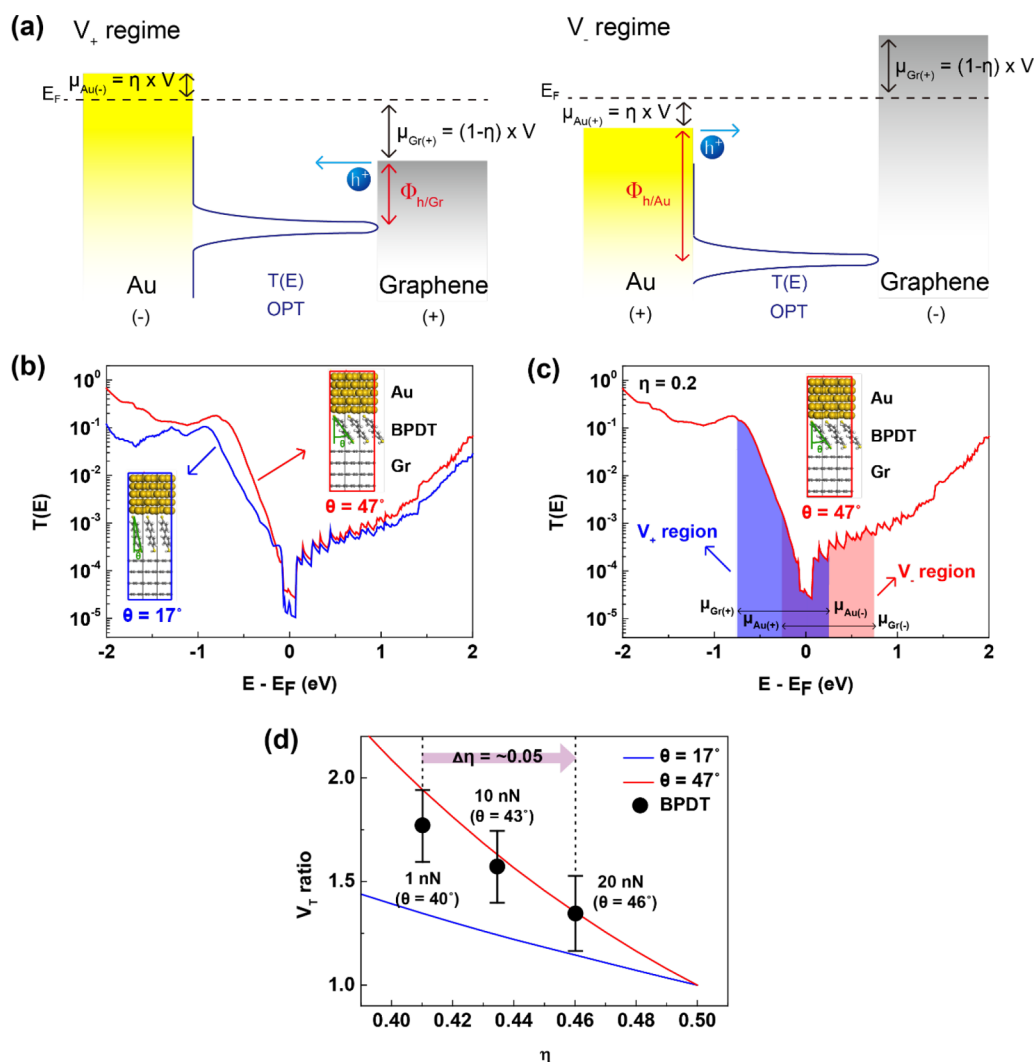


**Figure 4.** (a) Schematics of the energy-level alignments for the Au/OPT SAMs/graphene junction that illustrate the different voltage drops at both interfaces depending on the voltage polarities ( $V_+$  and  $V_-$  regions) and a  $\eta$ . Note that  $\mu_{\text{Gr}} = (1 - \eta)V$  at graphene and  $\mu_{\text{Au}} = \eta V$  at Au. The blue curves represent a  $T(E)$  corresponding to the HOMO orbital. The  $\Phi_{\text{h/Gr}}$  and the  $\Phi_{\text{h/Au}}$  represent the hole-injection barrier heights under different voltage polarities, respectively. (b) DFT-based  $T(E)$  for Au/BPDT/graphene molecular junctions showing two different tilt angles [ $\theta = 17^\circ$  (blue) and  $47^\circ$  (red)]. (c) Integrated  $T(E)$  peak areas at  $\theta = 47^\circ$  in the  $V_+$  and  $V_-$  regions, indicated by blue and red, respectively. (d) Calculated and experimentally obtained  $V_T$  ratio– $\eta$  plots for BPDT molecular junction at  $\theta = 17^\circ$  and  $47^\circ$ . Blue and red solid lines show the estimated  $V_T$  ratio for  $\theta = 17^\circ$  and  $47^\circ$ , respectively, in the range of  $\eta = 0.39$ – $0.50$ . Molecular tilt-angles under different  $F_L$  were calculated from the Hertzian elastic contact model.  $\eta$  shifted from  $\sim 0.41 \pm 0.02$  to  $\sim 0.46 \pm 0.01$  when  $F_L$  was increased in the range of  $F_L \leq 20$  nN.

BPDT molecules near the  $E_F$  were calculated and analyzed using two different molecular-tilt configuration ( $\theta = 17^\circ$  and  $47^\circ$ ), as shown in Figure 3a. The molecular orbital peak extended further to  $E_F$  for  $\theta = 47^\circ$  than for  $\theta = 17^\circ$ , leading to better conductivity. It should be noted that the DOS area in the range  $|E - E_F| \leq 1$  was  $\sim 16.4\%$  larger for  $\theta = 47^\circ$  than for  $\theta = 17^\circ$ , implying stronger interfacial coupling between graphene and molecules at higher tilt angles. In other words, molecular orbitals could be more affected by the graphene electrode when  $\theta = 47^\circ$ , thereby widening the DOS. In addition, from the geometry optimization in which Au and graphene were fixed in Au-BPDT and BPDT-graphene-slab models, the bond between graphene and the molecular thiol ( $-\text{SH}$ ) anchoring group shortened from 3.02 to 2.85 Å at equilibrium when the molecular-tilt angle was increased from 17 to  $47^\circ$ . A shortened tunneling length can enhance tunneling transport. In contrast, the DOS of Au and the BPDT molecules barely changed in the range  $|E - E_F| \leq 1$  as  $\theta$  was increased from 17 to  $47^\circ$ , as shown

in Figure 3b. Furthermore, the bond between Au and the molecular ( $-\text{S}$ ) anchoring group barely shortened from 1.95 to 1.93 Å at equilibrium. In this sense, the decreased asymmetry might have originated from the stronger coupling between graphene and the BPDT molecules when the molecular structure was tilted to a higher angle.

From the assumption that all potential drops occur at junction interfaces, the energy-level alignments for the Au/OPT SAM/graphene junction can be schematically illustrated according to the applied voltage polarities ( $V_+$  and  $V_-$ ), as shown in Figure 4a.<sup>17</sup> When a finite voltage is applied, the potential drop occurs differently according to the location of the junction interface where the graphene and the Au electrode come into contact. Note that  $\mu_{\text{Gr}}$  and  $\mu_{\text{Au}}$  are the chemical potentials at junction interfaces, i.e.,  $\mu_{\text{Gr}(+)} = (1 - \eta) \times V$  for graphene and  $\mu_{\text{Au}(-)} = \eta V$  for Au in the  $V_+$  region ( $V > 0$ ), and  $\mu_{\text{Gr}(-)} = (1 - \eta) \times V$  for graphene and  $\mu_{\text{Au}(+)} = \eta V$  for Au in the  $V_-$  region ( $V < 0$ ; Figure 4a). For simplicity, it was also

assumed for this model that the voltage-drop asymmetry is identical to the contact-coupling asymmetry between the junction interfaces. Figure 4b shows DFT-based  $T(E)$  calculated as a function of  $E - E_F$  for BPDT molecular junctions showing  $\theta = 17$  (blue) and  $47^\circ$  (red). When  $\theta$  was changed from  $17$  to  $47^\circ$ , the first  $T(E)$  peak (related to the HOMO level) shifted from  $-0.93$  to  $-0.80$  eV, close to  $E_F$ . In addition, the  $T(E)$  peak for  $\theta = 47^\circ$  was broader than the one for  $\theta = 17^\circ$  in the transport regime. These may be due to the enhancement of the interfacial coupling between the molecule and graphene, as discussed in Figure 3. Because the  $V_T$  point in the  $F-N$  plot is one of the general features of tail integration of  $T(E)$  function,<sup>31</sup> the  $T(E)$  peak shifting close to the  $E_F$  and broadening can decrease  $V_T$ , in agreement with our experimentally obtained  $V_T$  results in the range of  $F_L \leq 20$  nN.

To estimate the  $V_T$  ratio and  $\eta$  for the different molecular-tilt configurations, the tunneling conductance ( $G$ ) was estimated from  $T(E)$ -based Landauer formalism ( $G \propto \int T(E)dE$ ). The integrated  $T(E)$  peak areas were calculated for  $\theta = 17^\circ$  and  $47^\circ$  and  $0.1 \leq \eta \leq 0.5$  in the  $V_+$  and  $V_-$  regions and are shown in Figure S8. Figure 4c shows a representative example of an integrated  $T(E)$  peak area plotted for  $\theta = 47^\circ$  and  $\eta = 0.2$  in the  $V_+$  and  $V_-$  regions marked by blue and red, respectively. It should be noted here that the range of the  $\eta$  is  $0 < \eta \leq 0.5$ , and the highest  $\eta$  ( $\eta = 0.5$ ) indicates the symmetric contact coupling at both interfaces. Using  $G$  and the relationship  $\ln(G) \propto -(\Phi_h)^{1/2}$ , known as the exponential dependence of  $G$  on molecular barrier  $\Phi_h$ , the  $\Phi_h$  ratio (or  $V_T$  ratio), defined as  $\Phi_{h/Au}/\Phi_{h/Gr}$ , can be estimated. When  $\eta$  is close to 0.5, the integrated  $T(E)$  peak area is decreased in the  $V_+$  region, indicating an increase in  $\Phi_{h/Gr}$ . Alternatively, the integrated  $T(E)$  peak area is increased in the  $V_-$  region, indicating a decrease in  $\Phi_{h/Au}$  (Figure S8). Consequently, the  $\Phi_h$  ( $V_T$ ) ratio can be decreased when  $\eta$  is increased. The solid lines in Figure 4d exhibit the estimated  $V_T$  ratios plotted as functions of  $\eta$  for the BPDT molecular junctions tilted at  $\theta = 17$  (blue) and  $47^\circ$  (red), respectively. From the assumption that  $T(E)$  linearly shifts close to  $E_F$  as  $\theta$  is increased from  $17$  to  $47^\circ$ , the  $V_T$  ratios and  $\eta$  corresponding to intermediate molecular-tilt configurations (i.e.,  $17^\circ < \theta < 47^\circ$ ) can be estimated (Figure S9). From the comparison of the theoretically estimated  $V_T$  ratios to the  $V_T$  ratios experimentally obtained at different  $F_L$  and  $\theta$ ,  $\eta$  for the BPDT molecular junction shifted from  $\sim 0.41 \pm 0.02$  to  $\sim 0.46 \pm 0.01$  as  $F_L$  ( $\theta$ ) was increased from  $1$  ( $\sim 40^\circ$ ) to  $20$  nN ( $\sim 46^\circ$ ; Figure 4d). The estimation of  $\theta$  as a function of  $F_L$  is included in Table S1. Because there is no particular difference between the  $V_T$  results obtained for the BPMT and BPDT molecular junctions,  $T(E)$  for the BPMT molecular junction presumably shows similar  $\theta$ -dependent behavior. We also demonstrated that the  $V_T$  ratio calculated from the molecular coherent model<sup>29</sup> considering of differently weighted  $T(E)$  depending on the  $\theta$ , which is also in good agreement with our experimental results (Figure S10).

However, it is notable that the vdW interaction between the aromatic molecular structures (i.e., the series of phenyl rings) became stronger when the molecules were more tilted due to the increase of the  $F_{vdW}$  between the phenyl rings, which could play a role in the limiting of the molecular-tilt configuration. It has actually been reported that longer alkyl molecules are less tilted under the same  $F_L$  because the longer alkyl chain with its higher  $F_{vdW}$  is more resistant to the tip stress than the shorter one.<sup>15</sup> In addition, the increasing of the width of the tunneling current in the conjugation-based molecular junction according

to the  $F_L$  was further limited due to a stronger vdW interaction between the conjugated molecules compared to the alkyl structure.<sup>32</sup>

To quantitatively estimate the  $F_{vdW}$  between the OPT molecules, the intergraphene equilibrium distance and its vdW interaction were considered because the orbital structure of the phenyl ring is similar to that of graphene that consists of sp<sup>2</sup>-hybridized carbon atoms.<sup>33</sup> The well-known typical equilibrium-spacing distances of multilayer graphene are  $\sim 3.35$  Å, as shown in Figure 5a.<sup>34</sup> At spacing distances less than this, the  $F_{vdW}$  could dominantly act between the graphene layers. Similarly, it was assumed that the similar  $F_{vdW}$  will act between

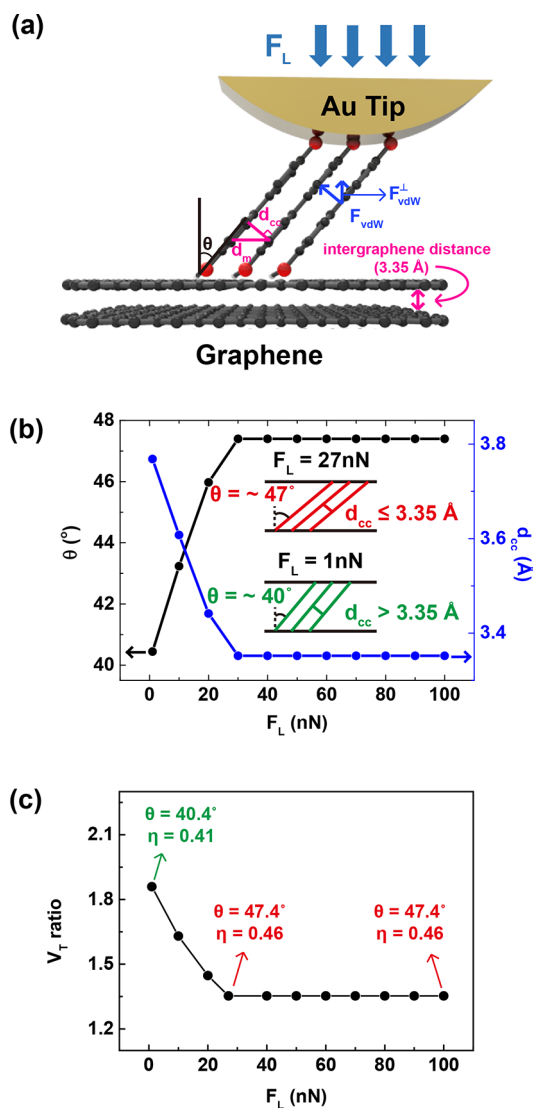


**Figure 5.** (a) Schematic of the Au/OPT SAMs/graphene junction with the intergraphene distance ( $\sim 3.35$  Å),  $\theta$ ,  $d_{cc}$ ,  $F_{vdW}$ , and  $F_{vdW}^L$  as the  $F_L$  is applied. (b) Plots of  $\theta$  and  $d_{cc}$  as a function of  $F_L$ . Insets show the schematic of the inter-electrode molecular-tilt configurations depending on the  $\theta$  and the  $F_L$ . At  $F_L = 1$  nN, the  $\theta$  and the  $d_{cc}$  were estimated to  $40.4^\circ$  and  $3.77$  Å, respectively. At  $F_L = 27$  nN, the  $\theta$  and the  $d_{cc}$  were estimated to be  $47.4^\circ$  and  $3.35$  Å, respectively. (c) The calculated  $V_T$  ratio with respect to  $F_L$  considering  $\eta$ ,  $\theta$ , and intermolecular  $F_{vdW}^L = 171$  nN at  $\theta = 47.4^\circ$ . Note that it was assumed that  $\eta$  shifted from  $\sim 0.41$  to  $\sim 0.46$ , and the  $\theta$  is changed from  $40.4^\circ$  to  $47.4^\circ$ , when  $F_L$  was increased from  $1$  to  $27$  nN. When  $F_L \geq 27$  nN, the  $\eta$  is  $0.46$ , and the  $\theta$  is  $47.4^\circ$ .

the molecular layers when the intermolecular distance is close to  $\sim 3.35 \text{ \AA}$  at  $d_{cc} = d_m \times \cos \theta$ . Note that  $d_m$  is a nearest-neighbor spacing of molecules (see the [Methods](#) section). The average  $F_{vdW}$  per graphene unit cell that was obtained is  $\sim 0.45 \text{ nN}$ , and this can be estimated based on the slope of the layer–layer binding energy per surface unit cell versus the separation distance in the two graphene sheets.<sup>35</sup> Because the  $F_L$  of the Au tip approaches the top of a few hundred SAMs in the surface-normal direction, the normal component of the repulsive  $F_{vdW}$  ( $F_{vdW}^\perp$ ) will be generated from all of the contacted molecules in the junction at  $d_{cc} \leq 3.35 \text{ \AA}$  (corresponding to  $\theta \geq 47.4^\circ$ ) at the same degree (if the total  $F_{vdW}^\perp > F_L$ ), leading to an attenuation of the degree of the change of the molecular-tilt angle ( $\Delta\theta$ ) ([Figure 5a](#)). With these assumptions, the  $F_{vdW}^\perp$  can be simply estimated by  $F_{vdW}^\perp = 2 \times 0.45 \text{ nN} \times \sin(47.4^\circ) \times$  the number of molecules ( $\sim 258$ ), where the factor 2 indicates 1 phenyl rings per molecule. The calculated  $F_{vdW}^\perp$  is  $\sim 171 \text{ nN}$ , which is much higher than the maximum applied  $F_L = 100 \text{ nN}$ . It was assumed that one molecule can only generate a single  $F_{vdW}^\perp$ . Note that the dependency of the number of molecules that are contained in the junction on the  $F_L$  is explained in the [Methods](#) section and [Table S1](#). In this result, it is difficult to further tilt the molecules ( $\theta \geq 47.4^\circ$ ), and the  $d_{cc}$  cannot be less than  $3.35 \text{ \AA}$  if the  $F_{vdW}^\perp > F_L$ . In consideration of the intermolecular  $F_{vdW}^\perp$ , the specific  $F_L$  of  $27 \text{ nN}$  that makes  $\theta = \sim 47.4^\circ$  and  $d_{cc} \approx 3.35 \text{ \AA}$  can be found using the Hertzian elastic-contact model,<sup>14,15,36</sup> as shown in [Figure 5b](#) and [Table S1](#).

When the  $F_L \geq 27 \text{ nN}$ , the molecular-tilt configuration is no longer changed by the  $F_L$  due to the larger intermolecular  $F_{vdW}^\perp$ , while in the case of  $F_L < 27 \text{ nN}$ , sufficient space exists to change the molecular-tilt configuration, which is shown in [Figure 5b](#). Therefore, the  $T(E)$  shift and its broadening can be limited according to the magnitude of the  $F_L$ , causing the constant  $V_T$  ratio in [Figure 2](#) at  $20 \text{ nN} \leq F_L \leq 100 \text{ nN}$ . [Figure 5c](#) shows the calculated  $V_T$  ratio as a function of  $F_L$  considering  $\eta$ ,  $\theta$ , and intermolecular  $F_{vdW}^\perp$ . Similar to the experimental  $V_T$  ratio, they also show two distinct transport regimes according to the  $F_L$  dependence ( $F_L < 27 \text{ nN}$  versus  $F_L \geq 27 \text{ nN}$ ). In addition, the theoretical  $V_T$  ratio with respect to  $F_L$  in [Figure 5c](#) was reduced from 1.86 to 1.35 when  $F_L$  was increased from 1 to  $27 \text{ nN}$ , while it was almost independent of the  $F_L$  magnitude at the  $F_L \geq 27 \text{ nN}$  and found to be 1.35, in agreement with our experimentally obtained results of [Figure 2c,d](#).

**Conclusions.** In this study, the variability of the molecular orbital alignment that is associated with the correlation effect between the asymmetry at the contacts, the molecular-tilt configuration, and the intermolecular vdW interaction was investigated and modeled, causing the  $F_L$ -dependent and  $F_L$ -independent tunneling. In particular, the reduction of the  $V_T$  ratio in the  $F_L$ -dependent regime is due to the enhancement of the physisorbed contact coupling between graphene and OPT molecules as the  $F_L$  was increased, leading to the increase of the  $\eta$ . Furthermore, the  $F_L$ -independent transport behaviors (the asymmetric ratio of the tunneling currents or  $V_T$  ratio), indicating a sustainable asymmetric coupling, were originated from the molecular-tilt configuration limited by the intermolecular vdW force. In other words, the dependence of rectification and conductance on tilt angle is robust to the number of molecules in the junction, and the primary effect of vdW forces is to constrain the possible tilt angles. Because one of the motivations for exploring single-molecule transport is to

develop bottom-up approaches to designing molecular electronics, this is an important connection to the stress. The present study will provide a comprehensive understanding of the correlational effect of the junction asymmetry, the molecular-tilt configuration, and the vdW interaction between the aromatic molecules on the molecular orbital alignment in a molecular-scale junction.

**Methods. Sample Preparation.** To fabricate the molecular junction, approximately three layers of exfoliated graphene film were prepared on an Au (50 nm)/Cr (5 nm)/ SiO<sub>2</sub>/Si substrate using the micromechanical-cleavage method, and this was utilized as the bottom electrode. The graphene structure was confirmed using Raman spectra ([Figure S11](#)). Note that it is expected that the exfoliated graphene can relatively avoid the unwanted interfacial variations compared to the chemical vapor deposition (CVD)-grown graphene that potentially includes many metallic/nonmetallic contaminations and grain boundaries.<sup>37</sup> To form the densely packed molecular SAMs on the Au tip, the tip was immersed in the OPT solutions ( $\sim 5\text{-mM}$  ethanol) for approximately several hours in a nitrogen-gas (N<sub>2</sub>)-filled glovebox with less than approximately 10 ppm of O<sub>2</sub>. In addition, the SAM deposition method, by chemical vapor deposition from a crucible at  $60^\circ \text{C}$  for 1 h 30 min, was used to form the lower-packing-density BPMT SAMs on the Au tip.<sup>38</sup> To remove the nonassembled residual molecules from the Au tip, the tip was rinsed with ethanol and was blown using N<sub>2</sub>.

**Electrical Characterization.** The Au tip that had been coated with the molecules was carefully placed at the bottom graphene electrode with a specific  $F_L$  using the CAFM technique for which the Park NX10 was utilized (Park Systems Corp., South Korea). For the electrical measurement, the Au tip was set as a ground, and voltages were applied on the graphene electrode. The  $I$ – $V$  electrical characteristics were measured at a stationary mode under various  $F_L$  values with the DLPCA-2000 built-in current amplifier (Electro Optical Components) at a humidity of  $<15\%$ . To obtain statistically meaningful data, the electrical measurements were repeatedly performed at different junction positions (at least 35–50 times).

**Estimated Number of Contacted Molecules.** For the densely packed OPT SAMs on the Au (111) surface, the well-known ordered  $\sqrt{3} \times \sqrt{3}R30^\circ$  (Wood's notation) structure of the closed packed molecules with a tilt angle of  $\theta = 17^\circ$  and a nearest-neighbor spacing of  $d_m = 4.95 \text{ \AA}$ , which yields a grafting density of  $N_o \approx 4.08 \times 10^{18} \text{ m}^{-2}$ , was adopted.<sup>39</sup> Several reports have indicated that biphenylenethiol molecules showed tilt angle configurations in the range  $17$ – $30^\circ$ .<sup>38–41</sup> The variation might arise from different Au substrate crystalline orientations, different synthesis temperatures, or different methods of synthesizing SAM on Au (i.e., vapor deposition or solution processing).<sup>38–41</sup> For the simplicity of the theoretical calculations, we assumed highly compact monolayers and  $\theta \approx 17^\circ$ .<sup>39</sup> Because the scanning electron microscopic (SEM) investigation showed an Au-tip radius of  $\sim 30 \text{ nm}$ , and the contact radius was calculated as  $\sim 3.73 \text{ nm}$  at  $F_L = 1 \text{ nN}$  using the Hertzian elastic-contact model, the estimated number of molecules that are contained in the junction is  $\sim 178$  ([Figure S12](#) and [Table S1](#)). It should be noted here that a higher  $F_L$  can increase the net-loading force ( $P_n = F_L +$  adhesion force) and the contact radius, thereby resulting in an increase of the number of contacted molecules

in the junction, and this is summarized in Table S1, while the details are explained in the Supporting Information.

**DFT Calculation.** A pair of tilt configurations of Au/BPDT/graphene junction were modeled by periodic hexagonal cells composed of a five-layer Au(111) slab, a four-layer graphite (0001) slab, and tilted BPDT whose thiolate (–S) and thiol (–SH) groups are bound to hollow sites of Au and graphene, respectively (Figure 4b, inset). The geometry was optimized with the Perdew–Bruke–Ernzerhof functional, the Grimme D3 dispersion correction, the SG15 optimized norm-conserving pseudopotential and medium-level numerical atom-centered basis set, a real-space grid whose density is equivalent to a plane-wave kinetic energy cutoff of 185 Ry, and the  $6 \times 6 \times 1$  Monkhorst–Pack k-point grid, as implemented in the ATK 2017.2 code. (References are listed in the Supporting Information). At the optimized geometry (described in detail in the Supporting Information), the DOS curves of BPDT/graphene and Au/BPDT partial models were calculated at  $18 \times 18 \times 1$  k points (Figure 3a,b), and the  $T$  curves of the full models were calculated at  $36 \times 36 \times 100$  k points with the nonequilibrium Green's function formalism (Figure 4).

## ■ ASSOCIATED CONTENT

### Supporting Information

The Supporting Information is available free of charge on the ACS Publications website at DOI: 10.1021/acs.nanolett.8b01294.

Additional details on  $I$ – $V$  characteristics and  $F$ – $N$  plots for the Au tip/BPMT/graphene, the Au tip/BPDT/graphene, and the Au tip/BPDT/Au molecular junctions; electrical characteristics; DOS and DFT-calculated  $T(E)$  for Au/BPDT/graphene molecular junction models; estimated  $V_T$  ratio- $\eta$  plots; optical image, atomic force microscopy (AFM) mapping data, and Raman spectroscopy of the three layers of graphene; SEM images; and tHertzian elastic contact model. (PDF)

## ■ AUTHOR INFORMATION

### Corresponding Authors

\*E-mail: gunukwang@korea.ac.kr.

\*E-mail: yhjjang@dgist.ac.kr.

### ORCID

Jaeho Shin: 0000-0002-7739-7195

Takhee Lee: 0000-0001-5988-5219

Yun Hee Jang: 0000-0002-6604-5813

Gunuk Wang: 0000-0001-6059-0530

### Author Contributions

G.W. conceived the project and J.S. designed, carried out, and analyzed the experiments; together, they wrote the paper. K.G. and Y.H.J. contributed to the theoretical calculations; S.Y. contributed to the sample preparation and measurements of graphene properties; C.L. and T.L. contributed to the data analysis; and J.S., Y.H.J., and G.W. revised the manuscript and led the effort to completion.

### Notes

The authors declare no competing financial interest.

## ■ ACKNOWLEDGMENTS

This work was accomplished with financial support from the National Research Foundation of Korea grant nos. 2017R1D1A1B03035441, 2016R1A2B4009037, 2016R1C1B2007330, and 2017R1A5A1014862 (SRC Program: vdWMRC Center), the National Creative Research Laboratory Program (grant no. 2012026372), the KU-KIST research fund, and the Korea University Future Research Grant. In particular, we appreciate Prof. Taekyeong Kim for discussion and comments on our results.

## ■ REFERENCES

- (1) Chen, J.; Reed, M. A.; Rawlett, A. M.; Tour, J. M. *Science* **1999**, *286*, 1550–1552.
- (2) Nitzan, A.; Ratner, M. A. *Science* **2003**, *300*, 1384–1389.
- (3) Beebe, J. M.; Kim, B.; Gadzuk, J.; Frisbie, C. D.; Kushmerick, J. G. *Phys. Rev. Lett.* **2006**, *97*, 026801.
- (4) Ohara, M.; Kim, Y.; Yanagisawa, S.; Morikawa, Y.; Kawai, M. *Phys. Rev. Lett.* **2008**, *100*, 136104.
- (5) Song, H.; Kim, Y.; Jang, Y. H.; Jeong, H.; Reed, M. A.; Lee, T. *Nature* **2009**, *462*, 1039–1043.
- (6) Kim, B.; Choi, S. H.; Zhu, X.-Y.; Frisbie, C. D. *J. Am. Chem. Soc.* **2011**, *133*, 19864–19877.
- (7) Gobbi, M.; Pietrobon, L.; Atxabal, A.; Bedoya-Pinto, A.; Sun, X.; Golmar, F.; Llopis, R.; Casanova, F.; Hueso, L. E. *Nat. Commun.* **2014**, *5*, 4161.
- (8) Xie, Z.; Báldea, I.; Smith, C. E.; Wu, Y.; Frisbie, C. D. *ACS Nano* **2015**, *9*, 8022–8036.
- (9) Campbell, I.; Rubin, S.; Zawodzinski, T. A.; Kress, J. D.; Martin, R. L.; Smith, D. L.; Barashkov, N. N.; Ferraris, J. P. *Phys. Rev. B: Condens. Matter Mater. Phys.* **1996**, *54*, R14321.
- (10) Repp, J.; Meyer, G.; Stojković, S. M.; Gourdon, A.; Joachim, C. *Phys. Rev. Lett.* **2005**, *94*, 026803.
- (11) Wang, G.; Kim, T.-W.; Jang, Y. H.; Lee, T. *J. Phys. Chem. C* **2008**, *112*, 13010–13016.
- (12) Quek, S. Y.; Venkataraman, L.; Choi, H. J.; Louie, S. G.; Hybertsen, M. S.; Neaton, J. B. *Nano Lett.* **2007**, *7*, 3477–3482.
- (13) Venkataraman, L.; Klare, J. E.; Nuckolls, C.; Hybertsen, M. S.; Steigerwald, M. L. *Nature* **2006**, *442*, 904–907.
- (14) Song, H.; Lee, H.; Lee, T. *J. Am. Chem. Soc.* **2007**, *129*, 3806–3807.
- (15) Wang, G.; Kim, T.-W.; Jo, G.; Lee, T. *J. Am. Chem. Soc.* **2009**, *131*, 5980–5985.
- (16) Frederiksen, T.; Munuera, C.; Ocal, C.; Brandbyge, M.; Paulsson, M.; Sanchez-Portal, D.; Arnau, A. *ACS Nano* **2009**, *3*, 2073–2080.
- (17) Kim, T.; Liu, Z.-F.; Lee, C.; Neaton, J. B.; Venkataraman, L. *Proc. Natl. Acad. Sci. U. S. A.* **2014**, *111*, 10928–10932.
- (18) Comstock, M. J.; Levy, N.; Kirakosian, A.; Cho, J.; Lauterwasser, F.; Harvey, J. H.; Strubbe, D. A.; Frechet, M. J.; Trauner, D.; Louie, S. G.; Crommie, M. F. *Phys. Rev. Lett.* **2007**, *99*, 038301.
- (19) Choi, J. W.; Flood, A. H.; Steuerman, D. W.; Nygaard, S.; Braunschweig, A. B.; Moonen, N. P.; Laursen, B. W.; Luo, Y.; DeIonno, E.; Peters, A. J.; Jeppesen, J. O.; Xu, K.; Stoddart, J. F.; Heath, J. R. *Chem. - Eur. J.* **2006**, *12*, 261–279.
- (20) Lauhon, L.; Ho, W. *J. Chem. Phys.* **1999**, *111*, 5633–5636.
- (21) Qi, Y.; Ratera, I.; Park, J. Y.; Ashby, P. D.; Quek, S. Y.; Neaton, J. B.; Salmeron, M. *Langmuir* **2008**, *24*, 2219–2223.
- (22) Kim, Y.; Song, H.; Strigl, F.; Pernau, H.-F.; Lee, T.; Scheer, E. *Phys. Rev. Lett.* **2011**, *106*, 196804.
- (23) Bruot, C.; Hihath, J.; Tao, N. *Nat. Nanotechnol.* **2012**, *7*, 35–40.
- (24) Nerngchamnong, N.; Yuan, L.; Qi, D.-C.; Li, J.; Thompson, D.; Nijhuis, C. A. *Nat. Nanotechnol.* **2013**, *8*, 113–118.
- (25) Slowinski, K.; Chamberlain, R. V.; Miller, C. J.; Majda, M. *J. Am. Chem. Soc.* **1997**, *119*, 11910–11919.

- (26) Beebe, J. M.; Kim, B.; Frisbie, C. D.; Kushmerick, J. G. *ACS Nano* **2008**, *2*, 827–832.
- (27) Wang, G.; Kim, Y.; Choe, M.; Kim, T. W.; Lee, T. A. *Adv. Mater.* **2011**, *23*, 755–760.
- (28) Wen, Y.; Chen, J.; Guo, Y.; Wu, B.; Yu, G.; Liu, Y. *Adv. Mater.* **2012**, *24*, 3482–3485.
- (29) Huisman, E. H.; Guédon, C. M.; van Wees, B. J.; van der Molen, S. J. *Nano Lett.* **2009**, *9*, 3909–3913.
- (30) Wang, G.; Kim, Y.; Na, S.-I.; Kahng, Y. H.; Ku, J.; Park, S.; Jang, Y. H.; Kim, D.-Y.; Lee, T. J. *Phys. Chem. C* **2011**, *115*, 17979–17985.
- (31) Araidai, M.; Tsukada, M. *Phys. Rev. B: Condens. Matter Mater. Phys.* **2010**, *81*, 235114.
- (32) Song, H.; Lee, C.; Kang, Y.; Lee, T. *Colloids Surf., A* **2006**, *284*, 583–588.
- (33) Novoselov, K. S.; et al. *Science* **2004**, *306*, 666–669.
- (34) Hod, O. *J. Chem. Theory Comput.* **2012**, *8*, 1360–1369.
- (35) Rydberg, H.; Dion, M.; Jacobson, N.; Schröder, E.; Hyltdgaard, P.; Simak, S. I.; Langreth, D. C.; Lundqvist, B. I. *Phys. Rev. Lett.* **2003**, *91*, 126402.
- (36) Johnson, K. L. *Contact Mechanics*; Cambridge University Press: Cambridge, United Kingdom, 1987.
- (37) Deokar, G.; Avila, J.; Razado-Colambo, I.; Codron, J.-L.; Boyaval, C.; Galopin, E.; Asensio, M.-C.; Vignaud, D. *Carbon* **2015**, *89*, 82–92.
- (38) Matei, D. G.; Muzik, H.; Golzhauser, A.; Turchanin, A. *Langmuir* **2012**, *28*, 13905–13911.
- (39) Sabatani, E.; Cohen-Boulakia, J.; Bruening, M.; Rubinstein, I. *Langmuir* **1993**, *9*, 2974–2981.
- (40) Tour, J. M.; Jones, L.; Pearson, D. L.; Lamba, J. S.; Burgin, T. P.; Whitesides, G. M.; Allara, D. L.; Parikh, A. N.; Atre, S. V. *J. Am. Chem. Soc.* **1995**, *117*, 9529–9534.
- (41) Azzam, W.; Wehner, B. I.; Fischer, R. A.; Terfort, A.; Woll, C. *Langmuir* **2002**, *18*, 7766–7769.